Materials Chemistry and Physics 329 (2025) 130058

Contents lists available at ScienceDirect

Materials Chemistry and Physics

journal homepage: www.elsevier.com/locate/matchemphys

Full Length Article

Optimization of pyroelectric figure of merit of PNN-PZ-PT composition at morphotropic phase boundary

Shubham Modgil [a], Mehak Aggarwal [a], Mukul Kumar [a], Arun Kumar Singh [b], Shobhna Dhiman [a], Gyaneshwar Sharma [c,*], Sanjeev Kumar [a,**]

[a] Physics Department, Punjab Engineering College (Deemed to be University), Chandigarh, 160012, India
[b] Electronics and Communications Engineering Department, Punjab Engineering College (Deemed to be University), Chandigarh, 160012, India
[c] Department of Physics, Tilak Dhari PG College, Jaunpur, 222002, India

GRAPHICAL ABSTRACT

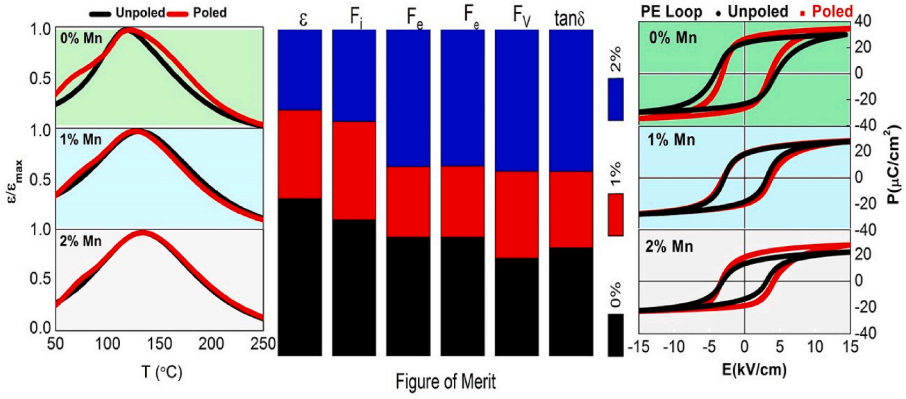

ARTICLE INFO

Keywords:
PNN-PZ-PT
Morphotropic phase boundary
Ferroelectrics
Pyroelectric

ABSTRACT

Ternary compounds are proven to be a more fascinating, owing to their potential to span a broader composition region of morphotropic phase boundary (MPB) – enhanced piezoelectric, electrostrictive, dielectric and ferroelectric properties. To activate defects dipoles, we perform MnO_2 doping in ternary MPB compound 0.55 $Pb(Ni_{1/3}Nb_{2/3})O_3$-0.135$PbZrO_3$-0.315$PbTiO_3$ [PNN-PZ-PT]. Temperature dependent dielectric spectroscopy reveals relaxor-ferroelectric nature of the synthesized ceramics. With the poling treatment, P-E loop of xMn-PNN-PZ-PT is softened, which emphasizes that the poling introduces higher order structural instability in MPB structure. The evolution of structural instability is as evidenced by the emergence of additional anomaly in thermal profile of dielectric constant due to electrical poling of xMn-PNN-PZ-PT and no systematic difference between polarizing behaviour of poled and unpoled specimen (Arrott plots). In association with defects dipoles, pyroelectric response based figure of merits (FOMs) of PNN-PZ-PT are improved. FOMs are characteristics of pyroelectric materials that insights about their suitability for specific application. F_i is suppressed with MnO_2 doping and F_v,

* Corresponding author.
** Corresponding author.
E-mail addresses: gyaneshwar.jnu@gmail.com (G. Sharma), sanjeev04101977@gmail.com, sanjeev@pec.edu.in (S. Kumar).

https://doi.org/10.1016/j.matchemphys.2024.130058
Received 13 July 2024; Received in revised form 5 October 2024; Accepted 15 October 2024
Available online 24 October 2024

F_e and F_e^* increases with MnO_2 doping. Our study reveals that tailored and precise acceptor doping is crucial for the simultaneous optimization of all pyroelectric FOMs.

1. Introduction

Piezoelectric materials find widespread applications in sectors like medical, naval and energy harvester [1,2]. Most piezoelectric ceramics also possess pyroelectric properties, allowing them to convert energy between thermal and electrical domains [3,4]. These materials are often used in the manufacturing of devices like actuators and sensing applications such as infrared detectors, intruder alarms, fire alarms, laser detectors, pollution monitoring devices, and thermal sensing applications [5–7]. Pyroelectric infrared detectors are very desirable due to their broad temperature range, affordability, low energy consumption, and strong stability. In addition to the pyroelectric coefficient, figures of merit (FOMs) are important for evaluating potential materials for pyroelectric detector devices including the current responsivity (F_i) FOM define as the amount of pyroelectric current (i_p) generated per watt of incident radiation power (W) on the pyroelectric element i.e. $F_i = i_p / W$ and voltage responsivity (F_v) FOM define as the amount of pyroelectric voltage (v_p) generated per watt of incident power i.e. $F_v = v_p / W$ [8,9]. Similarly, for energy harvesting application, two pyroelectric energy harvesting FOMs are defined i.e. F_e and F_e^*, where F_e is used for material selection for energy harvesting application and F_e^* is specifically used for devices exposed to a heat of specific energy density [10].

Lead-based pyroelectric materials, such as lead titanate [$PbTiO_3$, PT] and lead zirconate titanate [$Pb(Zr,Ti)O_3$, PZT], are commonly utilized in pyroelectric applications [11].These lead-based ferroelectrics follow a general formula of $Pb(B' B'')O_3$ where B′ represents Ni^{2+}, In^{3+}, Zn^{2+}, Mg^{2+}, Fe^{3+}, Mn^{4+}, Sc^{3+}, or Sn^{4+}; and B″ represents Ta^{5+}, Sb^{5+}, Nb^{5+} or W^{6+} [12,13]. Pure PZT and PT are often doped with other materials to enhance their properties and have shown significant results in systems like $Pb(Mg_{1/3}Nb_{2/3})O_3$-$PbTiO_3$ (PMN-PT), $Pb(Zn_{1/3}Nb_{2/3})O_3$-Pb(Zr,Ti)O_3 (PZN-PZT) and $Pb(Mg_{1/3}Nb_{2/3})O_3$-Pb(Zr,Ti)O_3 (PMN-PZT) [14–19].

Relaxor type ferroelectric, lead nickel niobate (PNN) is an important compound in the family of perovskite and has been studied by many researchers [20–23]. PNN possesses a pseudo cubic symmetry at room temperature and diffusive phase transition at −120 °C [24]. Since the discovery of PNN-PZ-PT ternary system by E.A. Buyanova et al., in 1965, its properties have been widely explored by many scientists [25–27]. PNN-PZ-PT based ceramics are well known for their excellent electromechanical coefficient (k_p), dielectric permittivity (ε), piezoelectric properties and pyroelectric properties [28–31].

The electrical properties of PNN-PZ-PT can be significantly altered by adding dopants. This modification is based on the defect chemistry inherent in the perovskite structure of PNN-PZ-PT. Introducing charged impurities can affect the concentration of oxygen vacancies within the material. These oxygen vacancies are crucial as they play a significant role in determining the electrical behaviour of the PNN-PZ-PT [32,33]. The incorporation of Mn can improve the sinterability of PZT-based ceramics by creating oxygen vacancies [34]. This is achieved through the dipole moment interaction between manganese ions and oxygen vacancies created by the substitution of B-site cation in perovskite lattice by a low valence manganese ion ($Mn^{3+}/^{2+}$) [35]. Studies have indicated that the doping of the Mn into PZT-based piezoelectric ceramics, introduces varying valence states of Mn due to the distinct heat treatments at different temperatures. Equation (1) gives the oxidation states of Mn stable at different temperature intervals [36].

$$\begin{matrix} & 535^{\circ}C\cdots 1080^{\circ}C\cdots 1650^{\circ}C & \\ MnO_2 & \rightarrow Mn_2O_3 \rightarrow Mn_3O_4 \rightarrow MnO & (1) \\ 4+\cdots & 3+\cdots 2+ 3+\cdots 2+ & \end{matrix}$$

It was also observed that, the incorporation of Mn into PZT results in improved pyroelectric properties [37]. Wei et al. [38] synthesized Mn doped $PbNb_{0.02}(Zr_{0.95}\ Ti_{0.05})_{0.98}O_3$ (PNZT95/5) ceramics and observed the high value of pyroelectric coefficient i.e, 9.15×10^{-8} C/cm^2. The enhancement of the pyroelectric property in PNMZT95/5 ceramics is due to Mn stabilizing internal polarization and reducing dielectric properties. Qiao et al. [39] investigated $(Pb_{1-1.5x}La_{0.02})(Zr_{0.86}Ti_{0.14})O_3$(x = 0.02, 0.03, 0.04 and 0.05)ceramics and discovered that x = 0.03 ceramic exhibit a high value of pyroelectric coefficient at room temperature i.e 5.2×10^{-8}C/cm^{2}K. The significant improvement of pyroelectric coefficient with increasing La doping is due to increase in metastable ferroelectric phase with applied electric field. K. Kang et al. [31] synthesized yttrium-doped 0.15[$Pb(Ni_{1/3}Nb_{2/3})O_3$]–0.85[$Pb(Zr_{1/2}Ti_{1/2})O_3$] ceramics and found that the maximum pyroelectric coefficient and figures of merit for undoped and 1.0 mol% Y^{3+} doped ceramics were 761 and 452 μC/m^2·K, respectively, at room temperature. The enhancement is attributed to formation of an extra phase within a material with higher Y^{3+} content.

Still there is no report available on pyroelectric properties of Mn doped PNN-PZ-PT. So, here in the present study, we examine how the

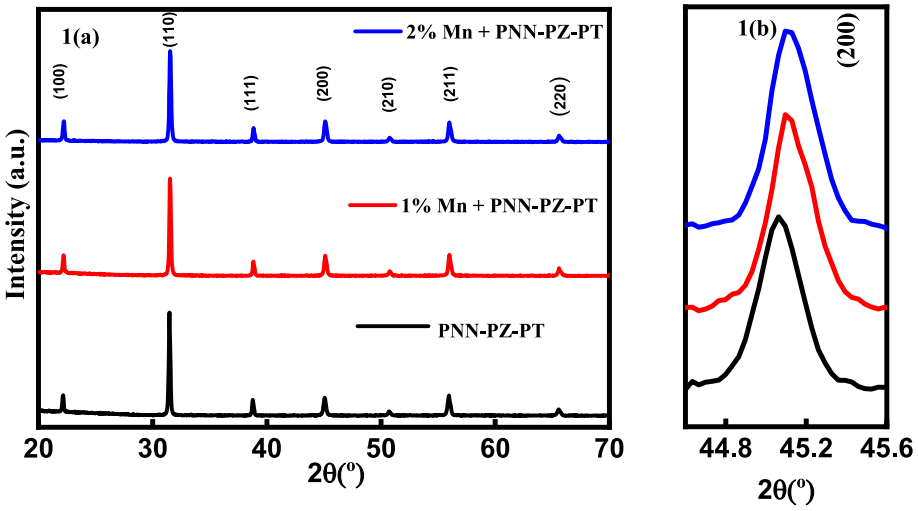

Fig. 1. (a) X-ray powders diffraction patterns of xMn-PNN–PZ–PT (x = 0 %, 1 % and 2 %), (b) Enlarged pattern correspond to 2θ = 44.6°–45.6°.

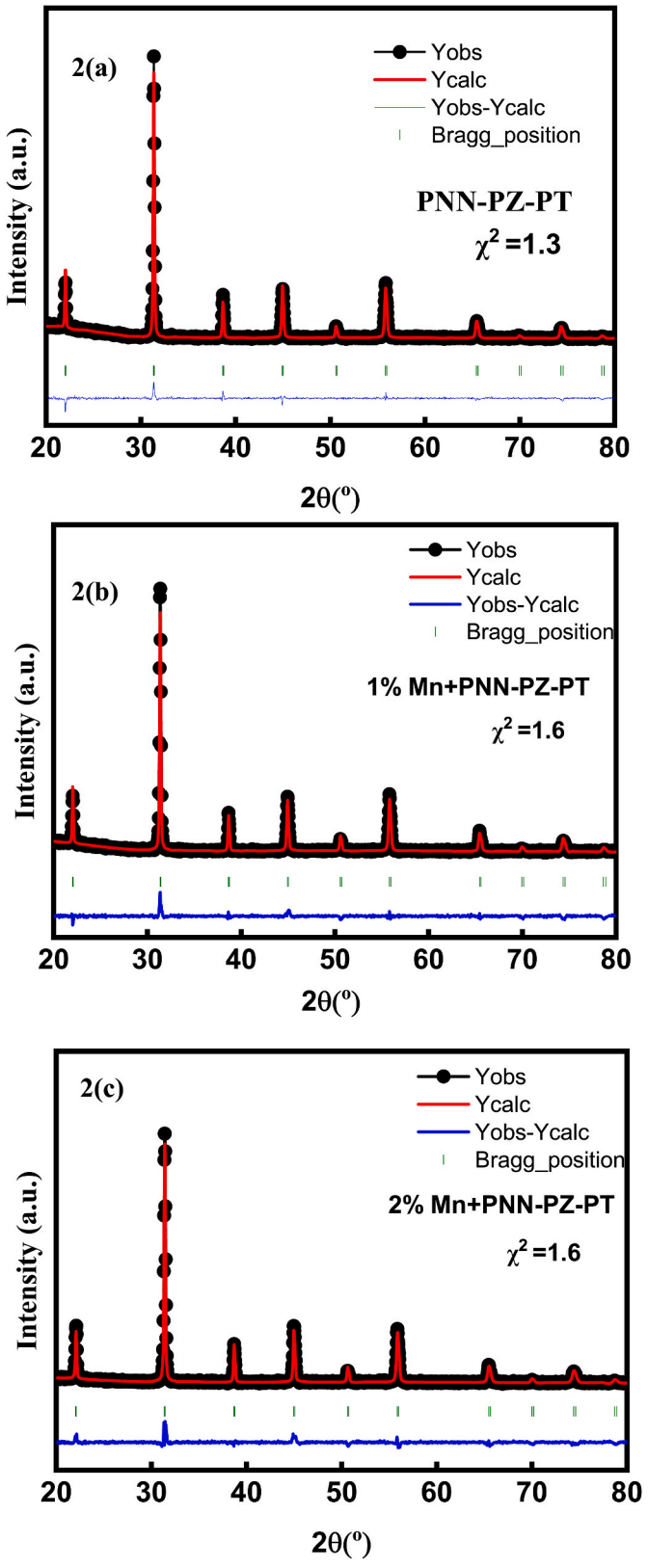

Fig. 2. (a–c) Rietveld refined XRD pattern for xMn-PNN-PZ-PT with (*Pm-3m*) structure models.

Table 1
Refinement parameters.

Composition	a (Å)	Volume ($Å^3$)	Density (g/cm^3)	Space group	χ^2
PNN-PZ-PT	4.0313	65.5156	8.287	Pm-3m	1.3
PNN-PZ-PT+1% Mn	4.0312	65.5094	8.289	Pm-3m	1.6
PNN-PZ-PT+2% Mn	4.0301	65.4552	8.305	Pm-3m	1.6

Table 2
Atomic parameters.

Pseudocubic (*Pm-3m*) structure parameters of xMn-PNN-PZ-PT ceramics				
Atomic coordinates	**x**	**y**	**z**	**Isotropic thermal parameters ($Å^2$)**
Pb	0.00000	0.00000	0.00000	1.00000
Ni/Nb/Zr/Ti/Mn	0.50000	0.50000	0.50000	1.00000
O	0.50000	0.00000	0.50000	1.00000

incorporation of MnO_2 impacts the structural, electrical and pyroelectric properties of the PNN-PZ-PT ceramics.

2. Experimental details

Polycrystalline ceramic specimens of 0.55PNN-0.135PZ-0.315 PT + xMnO_2 (x = 0, 1, and 2 mol%) were prepared using the conventional two step solid-state reaction method. Firstly, the precursor $NiNb_2O_6$ was synthesized by mixing the high purity raw powders of NiO(99.9 % Sigma Aldrich) and Nb_2O_5(99 %, Sigma Aldrich) and ball milling them in isopropyl alcohol (IPA) medium for 12 h (PM 400 Retsch) followed by calcination at 1000 °C for 6 h in a closed alumina crucible. This powder was again ball milled with PbO (99.9 % AlfaAesar), ZrO_2(99.9 %), TiO_2(99.9 %) and MnO_2(99.9 %) according to their stoichiometric ratio all chemicals were purchased from Sigma Aldrich. 1.0 wt% excess PbO was added to compensate the lead loss during calcination and sintering. The mixed powder was then calcined at 1050 °C for 4 h and re-milled for another 12 h. Green pellets were prepared by adding the 5 wt% PVA (Poly-vinyl alcohol) solution to the dried powder, and later pressed into disks with a diameter of 10 mm under 7 tons pressure using uniaxial pellet making hydraulic press. The PVA was burned off at 600 °C for 3 h and subsequently, the sintering of pellets was done at 1250 °C for 2 h. The sintered pellets were then polished to a thickness of 0.7 mm and silver electrodes were fired on both ends for further characterization. The X-ray diffraction (XRD) was carried out on X-ray diffractometer (PANalytical's X'Pert Pro) by crushing the sintered pellet into powder and annealing them at 600 °C for 30 min. The microstructural analysis of the samples was done using the field emission scanning electron microscope [FESEM, SU8010 SERIESHITACHI]. Dielectric studies temperature dependent were performed on the Impedance Analyzer [E4990A, KEYSIGHT]. The piezoelectric properties were performed on the sensor tech SS01 d_{33} m. The room temperature and temperature dependence ferroelectric studies (P-E Loop) were done using the Marine India P-E loop tracer.

3. Results and discussion

Fig. 1(a) shows the room temperature XRD patterns of the 0.55 Pb($Ni_{1/3}Nb_{2/3}$)O_3-0.135$PbZrO_3$-0.315$PbTiO_3$ +xMnO_2 (x = 0 %, 1 %, and 2 %) ceramic samples. All the samples exhibit a typical ABO_3 perovskite structure without any trace of pyrochlore phase (JCPDS, PDF#34–0103). The obtained XRD peaks indicate that the Mn completely diffused into the lattice of PNN-PZ-PT. The diffraction patterns in the 2θ range of 44°–46° corresponding to the (200) diffraction peak are enlarged respectively, in Fig. 1(b). In the present study, the

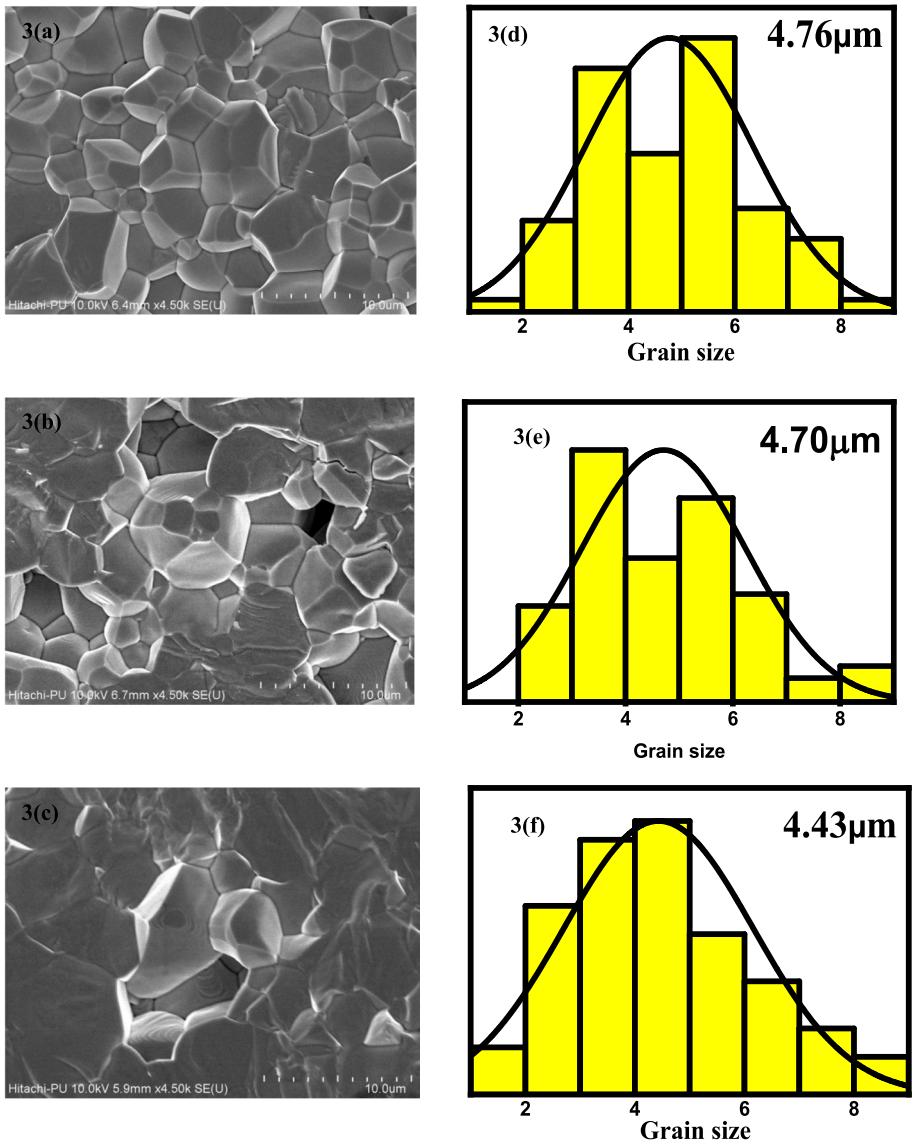

Fig. 3. (a–c) FESEM micrographs of xMn-PNN-PZ-PT(x = 0 %, 1 % and 2 %) ceramics, (d–f) average grain size.

sintering temperature for xMn-PNN-PZ-PT ceramics used is 1250 °C, which further results in manganese exits as Mn^{2+} (0.76 Å) or Mn^{3+} (0.58 Å), with Mn^{3+} being the predominant form [40]. The ionic radius of Mn^{3+} is smaller than that of Ti^{4+}(0.605 Å), which overall reduces the cell volume and results in shifting of peak towards higher angle with increasing Mn doping [41]. To investigate the structure of the prepared compositions, Rietveld refinement was performed using the FullProf software, and it reveals the presence of pseudo-cubic phase with *Pm-3m* space group as shown in Fig. 2(a–c). Tables 1 and 2 represent the different parameters such as lattice parameters, volume, density, space group and atomic parameters obtained using Rietveld refinement. It indicates that with Mn doping, cell volume decreases, which correlates with the shifting of XRD peaks toward higher angle. The Rietveld refinement of xMn-PNN-PZ-PT ceramics displays the best fit as the value of χ^2 for all samples is close to 1. It is also reported that ceramic compositions 0.55PNN–0.135PZ–0.315 PT at room temperature are considered near the coexistence of various phases i.e rhombohedral, tetragonal and pseudocubic symmetry [42,43]. Some reports also suggest the existence of monoclinic phase in PNN–PZ-PT and PNN–PT systems [44,45].

The FESEM micrographs of the fractured surface of xMn-PNN–PZ–PT (x = 0 %, 1 % and 2 %) ceramic pellets are shown in Fig. 3(a–c). All the images are shown at the same magnification and the grain size is calculated using the ImageJ software. The FESEM micrographs show the uniform grains with clear grain boundaries suggesting optimized sintering condition. The grain size generally followed a normal distribution, with the average size progressively decrease from 4.76 µm to 4.13 µm as the Mn doping content rose from 0 to 2 mol% as shown in Fig. 3 (d–f). By considering, the valence state and the principle of similar ionic radius, Mn^{3+} (0.58 Å) preferentially replaces Ti^{4+} (0.605 Å) from the B-site and results in the formation of oxygen vacancies [28]. The increase in oxygen vacancies at the grain boundary with increasing Mn content prevents the mobility of grain boundary and restricts the grain growth [46,47].

Fig. 4(a and b) represents the dielectric permittivity and dielectric loss of the as prepared ceramics as a function of temperature in the range 303 K–573 K with varying Mn content at 1 kHz. The value of dielectric permittivity for all xMn-PNN-PZ-PT samples rises with temperature displaying a peak attributing to phase transition. With the increase in Mn content, the value of dielectric permittivity decreases due to pinning effect, and the phase transition temperature (T_c) shifts towards high temperature [48]. This phenomenon occurs due to the emergence of oxygen vacancies generated from the doping of high-valance Ti^{4+} ion by the low-valence $Mn^{3+/2+}$ions. Along with oxygen vacancies, there is a

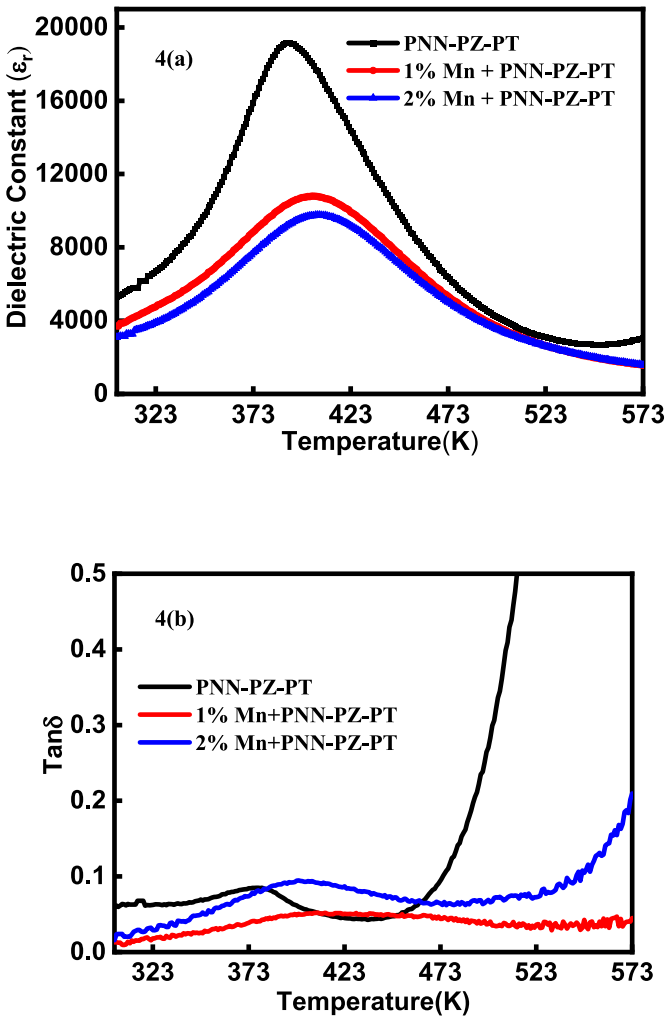

Fig. 4. (a–b) Temperature dependence of dielectric permittivity and dielectric loss for xMn + PNN-PZ-PT (x = 0 %, 1 % and 2 %).

formation of Mn_{Ti} acceptor centers, which further leads to the $(Mn_{Ti}\text{-}V_o^{\bullet\bullet})^{\times}$defect dipoles. These oxygen vacancies hinder the motion of domain wall by reducing the volume of perovskite cells [49].

Fig. 5(a) and (b) represent the dielectric permittivity (ε_r) and dielectric loss (tanδ) of PNN-PZ-PT ceramic with varying Mn content (x = 0 %, 1 % and 2 %) at the frequency range of 100 Hz −1 MHz. The value of dielectric permittivity was found to be almost equal for all the ceramics in the tested frequency range. The results also showed that the dielectric loss of Mn doped PNN-PZ-PT samples was lower compare to the pure ceramic sample. The room temperature dielectric loss for the 1 mol% Mn doped ceramic is ~0.0129 whereas, for the pure sample, the loss is around ~0.0585. The decrease in tanδ for x = 0.01 sample is attributed to the hardening effect of the acceptor dopant Mn [50]. However, x = 0.02 sample shows slightly high value of tanδ because of emergence of oxygen vacancies in the crystal structure. The amount of these vacancies increases with increase in Mn doping. Excessive oxygen vacancies become ionic charge carriers, leading to rise in dielectric loss for x = 0.02 sample [51]. It can also be observed from Fig. 4(a), that near Curie temperature (T_c) the shape of the dielectric curves showed a broader trend with the addition of Mn. To investigate the relaxor properties of the prepared ceramics, a graph between $\ln(1/\varepsilon_r\text{-}1/\varepsilon_{max})$ as a function of $\ln(T\text{-}T_{max})$ was plotted in Fig. 5(c). This plot follows the Uchino and Nomura function, also known as modified Curie-Weiss law [52].

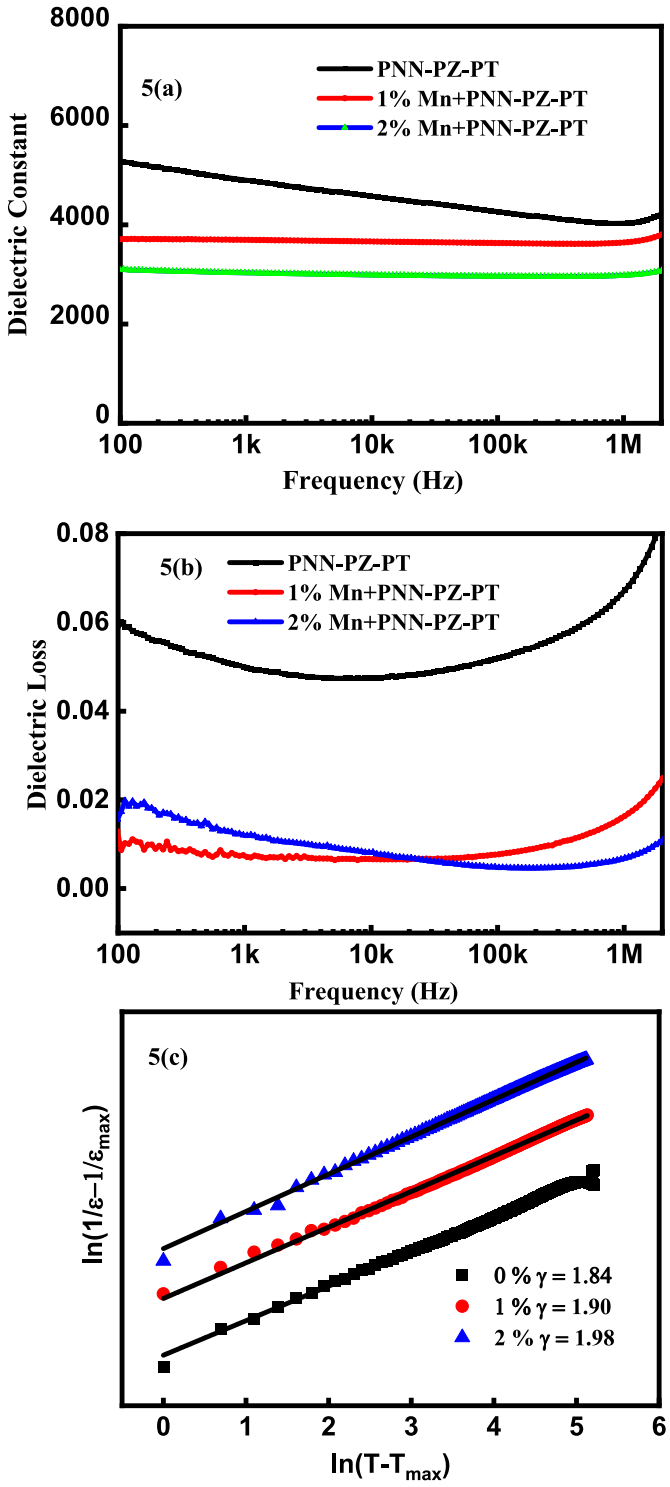

Fig. 5. (a)- Dielectric constant as the function of frequency at room temperature, (b)- dielectric Loss as the function of frequency at room temperature, (c)- $\ln(1/\varepsilon_r\text{-}1/\varepsilon_{max})$ plotted against $\ln(T\text{-}T_{max})$ at 1 kHz for the PNN–PZ-PT ceramics with various Mn content.

$$\left(\frac{1}{\epsilon_r}-\frac{1}{\varepsilon_{max}}\right)=\frac{(T\text{-}T_{max})^{\gamma}}{C} \quad (2)$$

where ε and ε_{max} represent dielectric permittivity and maximum dielectric permittivity respectively, at phase transition temperature (T_{max}), C is a constant, and degree of diffusiveness is represented by γ

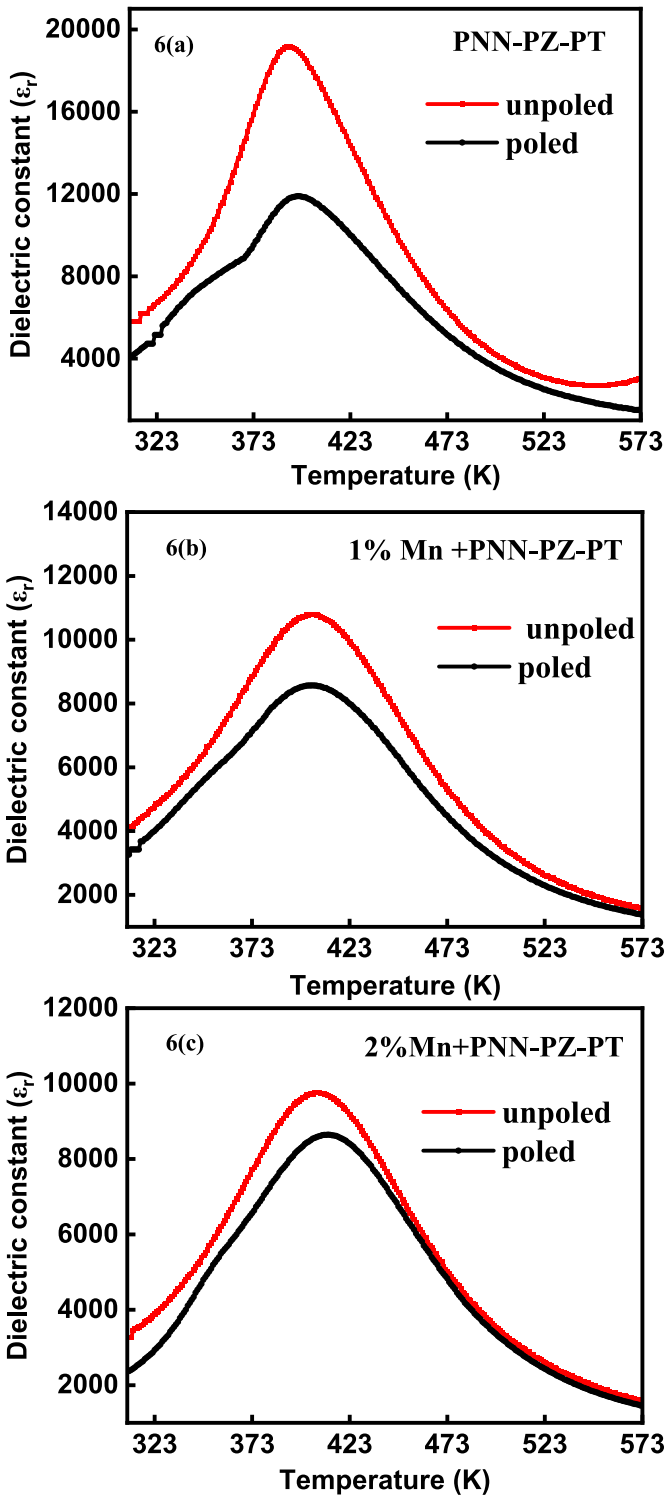

Fig. 6. (a–c) Dielectric permittivity variations with temperature for poled and unpoled xMn + PNN-PZ-PT ceramics.

whose range is between 1 and 2 ($\gamma = 1$ for normal ferroelectrics and $\gamma = 2$ is for relaxor ferroelectrics) [52]. By fitting the experimental data in modified Curie-Wiess law fitting yields the value of γ. The value of γ increases from 1.84 to 1.98 with the increase in Mn content, suggesting that the Mn doping enhances diffuse phase transition behaviour. To examine the effect of oxygen vacancy on ferroelectric phase transition, electric field poling was employed. The ceramics were subjected to a DC electric field at 3 kV/cm. Fig. 6(a–c) represents the $\varepsilon - T$ curve for poled and unpoled samples. The emergence of novel peak well below the transition temperature T_C is observed. The emergence of additional peaks evidences about the structure instability. Additionally due to poling process, the applied field aligns the defects dipole caused by oxygen vacancies, thereby decreasing their contribution to the dielectric constant [53].

Polarization (P) vs. electric field (E) is one of the important probing techniques and may be employed as a fingerprint to reveal the underlying complexity of a ferroelectric system. Fig. 7(a) represents the room temperature P-E loop of the PNN-PZ-PT + xMn (x = 0 %, 1 %, and 2 %) at 20 Hz. For x = 0 %, the ferroelectric loop is well saturated with remnant polarization, P_r ~23.37 μC/cm^2 and saturation polarization, P_s ~29.84 μC/cm^2. The P_r and P_s remarkably decrease with increasing Mn content because of the oxygen vacancies created by the substitution of Ti^{4+} by $Mn^{3+/2+}$ions. Such oxygen vacancies hinder the motion of domain walls and results in decreasing the value of remnant polarization [28].

Fig. 7(b–d) represents the P-E hysteresis loop, at room temperature, for the poled and unpoled ceramics. The figure clearly illustrates that the saturation polarization (P_s) and remnant polarization (P_r) values for the unpoled sample are lower compared to those of the poled samples. This observation suggests that the present scenario is more likely consistent with the structural instability, driven by electric field poling, as evidenced by $\varepsilon - T$ measurement for poled and unpoled samples. Asymmetric P-E loop characteristics are generally observed in an electrically poled hard ferroelectric. Shift in P-E loop on electric field axis arise from domain pinning and generate an internal bias field, E_i, equivalent to $\left(E_c^+ - E_c^-\right)/2$, depicts the presence of oriented defect dipoles. The defects dipoles are formed by the point defects and intentionally may be introduced by the doped ions with mixed valancy. During the poling process, defect dipoles are structurally coupled with macroscopic polarization, and their orientation is stabilized through oxygen vacancy mediated octahedral tilting or point defect migration [54], which further provide restoring forces via field E_i and retention to P_r [55]. Further, P-E loops of Mn-doped specimen (x = 1 % and 2 %) become asymmetric with poling. However, asymmetricity in P-E loop becomes more significant as Mn content increases. The E_i is found to be 0.19, 0.52, and 1.32 kV/cm for x = 0%, 1 % and 2 %, respectively. The emergence of the asymmetric P-E loop feature in $Mn^{3+/2+}$ doped specimen reveals the additional dynamics imposed by defect dipoles, led by the formation of oxygen vacancies. MnO_2 doping improves the formation of oxygen vacancies occurs as a result of substitution of higher Ti^{4+} with lower $Mn^{3+/2+}$ state. Table 3 represents the different values of parameters obtained from P-E loop.

We plot P^2 vs. E/P curves Fig. 8(a), known as Arrott plot, for electrically poled and unpoled specimens. The Landau free energy consideration in the vicinity of the transition temperature, free energy can be mentioned in terms of order parameter. In the condition of equilibrium, the minimization of free energy condition mathematically leads to a linear mathematical expression between P^2 and E/P. Both curves for all specimens are found to be linear and parallel, which suggests no additional difference between polarizing behaviour of the poled and unpoled specimen. This depicts that similar domain characteristics are observed during the removal of field, which further confirms that the splitting of Arrott lines corresponding to poled and unpoled specimen is genuinely driven by structural instability rather than domain mobility [56].

The piezoelectric properties of xMn-PNN-PZ-PT ceramics at room temperature exhibit a declining trend with the addition of Mn represented in Fig. 9(a). Specifically, the d_{33} piezoelectric coefficient decreases from 545 pC/N for undoped (x = 0 %) ceramics to 370 pC/N for 1 % Mn doping and further to 360 pC/N for 2 % Mn doping (measured after 24 h of poling). This decline in d_{33} is correlated with decreases in both ε_r and P_r. With increasing Mn content, both ε_r and P_r weaken, leading to a corresponding decrease in d_{33}, as indicated by Equation (3) [57].

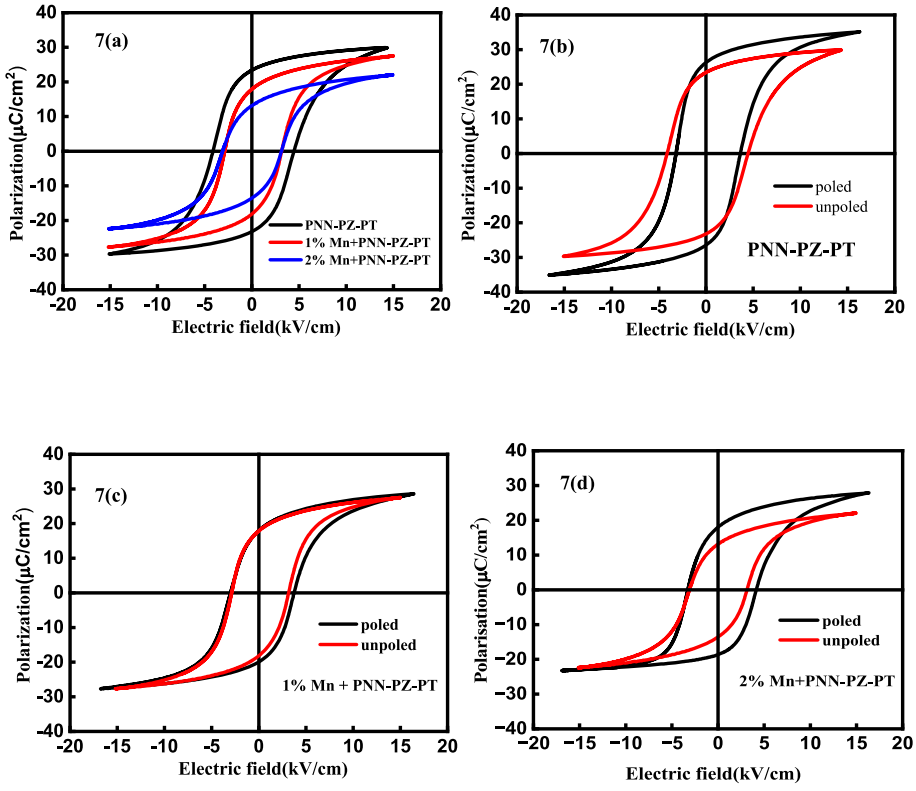

Fig. 7. (a) – P-E Loop of xMn + PNN-PZ-PT ceramics at room temperature at 20Hz frequency, (b–d) P-E Loop with and without polling.

Table 3
Ferroelectric properties of PNN-PZ-PT + xMnO2.

Composition	P_r (μC/cm^2)	P_s (μC/cm^2)	E_c (kV/cm)	E_i (kV/cm)
PNN-PZ-PT	23.37	29.84	4.45	0.19
PNN-PZ-PT+1%Mn	17.89	27.53	3.15	0.52
PNN-PZ-PT+2%Mn	13.14	22.03	3.13	1.32

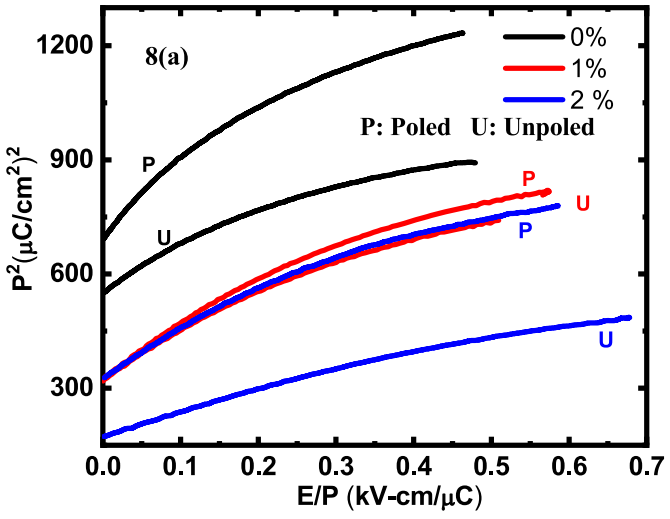

Fig. 8. (a) P^2 versus E/P plot for poled and unpoled xMn + PNN-PZ-PT ceramics.

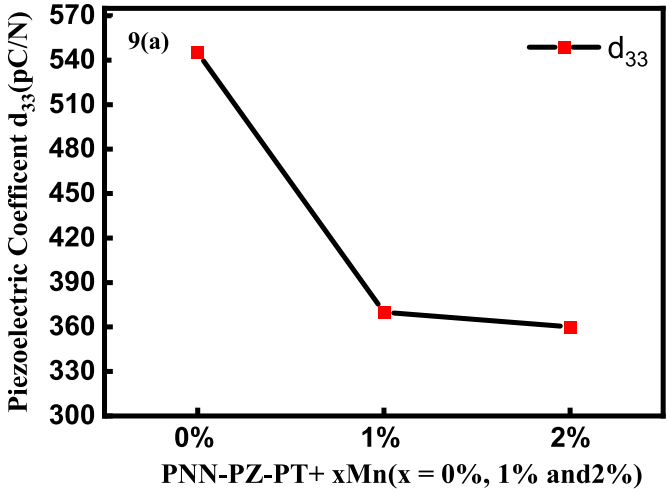

Fig. 9. (a) Variation of piezoelectric coefficient of xMn + PNN-PZ-PT ceramics at room temperature.

$$d_{33} = P_r \cdot \varepsilon_r \cdot Q \tag{3}$$

where Q is the electrostrictive coefficient.

To explore the pyroelectric properties of PNN-PZ-PT ceramics, P-E loops were measured at a series of temperature between 303K and 453K, providing an applied field of ±20 kV/cm at 20 Hz. From Fig. 10(a–c), it is observed that as temperature increases, the polarization diminishes consistently for all synthesized xMn-PNN-PZ-PT ceramics. Additionally, it reveals a decline in the values of P_s, P_r and E_c (coercive field) of xMn-PNN-PZ-PT ceramics with increasing temperature. This phenomenon is attributed to the increasing thermal agitation, which facilitates easier re-orientation of ferroelectric domains, consequently decreasing the

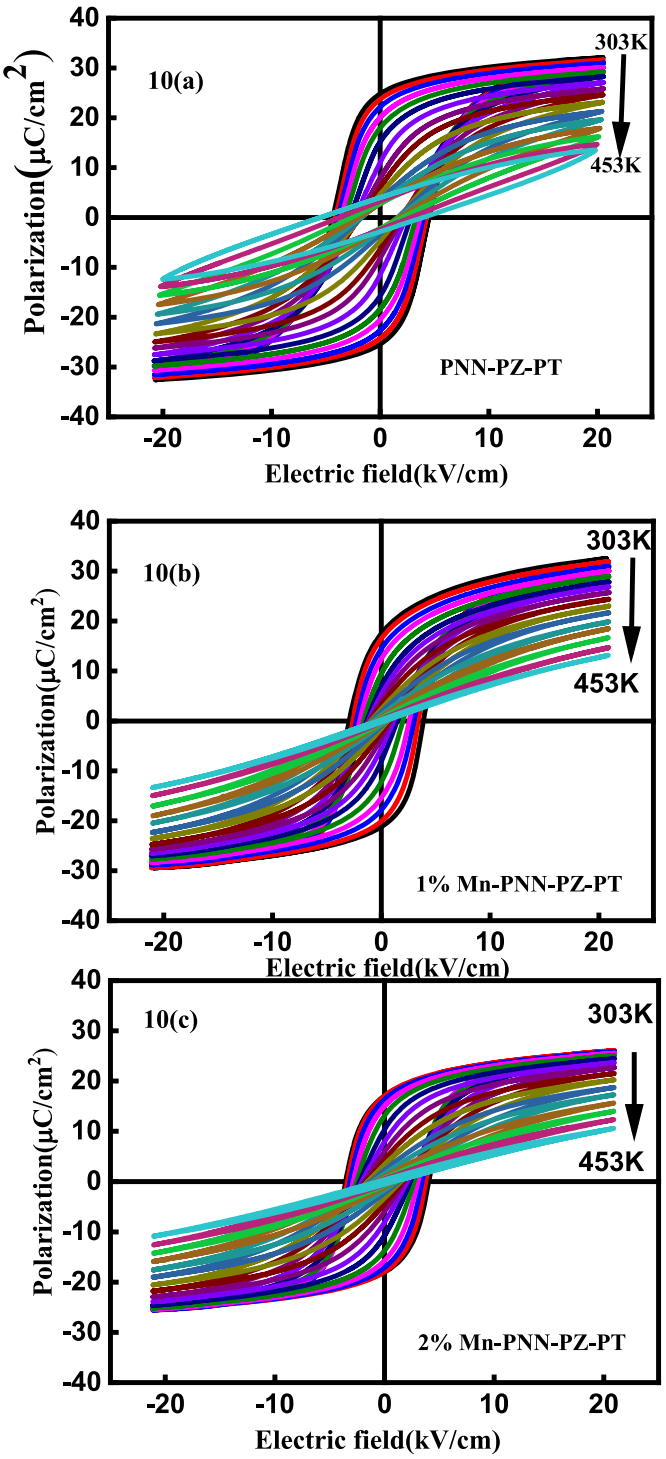

Fig. 10. (a–c) P-E Loop of the xMn + PNN-PZ-PT ceramics as the function of temperature ranging from (303 K–453 K) measured at 20Hz.

overall ferroelectric performance [58]. Fig. 11(a)–(c) depict polarization versus temperature (P-T) curves for all xMn-PNN-PZ-PT ceramics at different electric field strengths, derived from the isothermal P-E loops obtained at series of temperatures.

Fig. 11(d–f) displays the temperature dependence of pyroelectric coefficient, $\pi = dP/dT$, for xMn-PNN-PZ-PT ceramics at varying electric fields. The π in the vicinity of room temperature are found to be 10.632 $\times 10^{-4}$, 9.18 $\times 10^{-4}$, and 0.03 $\times 10^{-4}$ C m^{-2}K^{-1} for pure, 1 %, and 2 % Mn doped samples. Figure of merits (FOMs) are considered as decisive parameters towards their specific application. Here, we deal with FOMs F_i, F_v, F_e, and F_e^* that are mainly governed by pyroelectric coefficient & dielectric constant and used to estimate the performances of material as a component of pyroelectric sensing and energy harvesting devices. Doping approach may play a vital role in the performance of pyroelectric devices. Fig. 12(a–d) presents the thermal variation of the pyroelectric FOMs defined as [59]:

$$F_i = \frac{\pi}{C_v} \tag{4}$$

$$F_V = \frac{\pi}{C_v \varepsilon_0 \varepsilon_r} \tag{5}$$

$$F_e = \frac{\pi^2}{\varepsilon_0 \varepsilon_r} \tag{6}$$

$$F_e^* = \frac{\pi^2}{C_v^2 \varepsilon_0 \varepsilon_r} \tag{7}$$

here, C_v represents volume-specific heat, ε_r represents relative permittivity, and ε_0 signifies the permittivity of free space. The value of specific heat was taken from the literature [60].F_i, F_v, F_e and F_e^* represent current responsivity, voltage responsivity, and pyroelectric energy harvesting figure of merits, respectively. These FOMs help in choosing the materials for pyroelectric applications in various fields. The expression for FOMs indicates that higher values can be achieved by either increasing the pyroelectric coefficient or by decreasing the dielectric permittivity. However, there are various strategies to achieve high FOM values, such as chemical substitution (acceptor doping) [61], microstructural tuning by introducing porosity, and employing different synthesis techniques or by introducing defect dipoles [62–65]. Here, we adopt defect dipole route to optimize the pyroelectric performances of a ternary MPB compound. Pyroelectric coefficient is derived from P(E,T) vs T curves (Fig. 11(a–c)). From the thermodynamic consideration, in the vicinity of ferroelectric phase transition, order-parameter, P drops rapidly to attain zero value and as a result first order derivative of P, pyroelectric coefficient attains maximum value. Tables 4 and 5 represent the comparison table of FOMs of other well-known materials with the present work at room temperature and at elevated temperature [66–69]

For device application point of view, temperature dependence of FOMs has been evaluated for all xMn-PNN-PZ-PT ceramics, as shown in Fig. 12(a–d). As the pyroelectric figure of merit decreases with increase in Mn doping at room temperature, depicting a diminishing pyroelectric response. It leads to a significant drop for all FOMs at room temperature. However, at elevated temperature current responsivity FOM F_i is high for undoped sample but other FOMs i.e., F_v, F_e and F_e^* increases for 2 % Mn doped MPB specimen, indicating the higher pyroelectric response of 2 % doped sample, which occurs due to simultaneous suppression of $\pi - T$ and $\varepsilon - T$ curves with the Mn doping.

4. Conclusion

In conclusion, the present study systematically investigated the impact of Mn-doping on the structure, microstructure, dielectric, ferroelectric and pyroelectric properties of ternary MBP composition PNN-PZ-PT prepared by solid-state reaction method.These findings reveal that the addition of Mn additive has minimal effect on the structural properties. The partial substitution of Ti^{4+} cations by Mn^{3+} at the B-sites of a crystal structure of PNN-PZ-PT leads to the formation of oxygen vacancies, which results in decreased grain size with increasing Mn content. The dielectric spectroscopy analysis reveals that the synthesized ceramics exhibit diffusive characteristics, however the degree of diffuseness (γ) increases from 1.84 to 1.98 with increasing Mn content, suggesting relaxor behaviour. The splitting of Arrott lines corresponding to poled and unpoled specimen is driven by structural instability rather than domain mobility for all the ceramics. Notably the

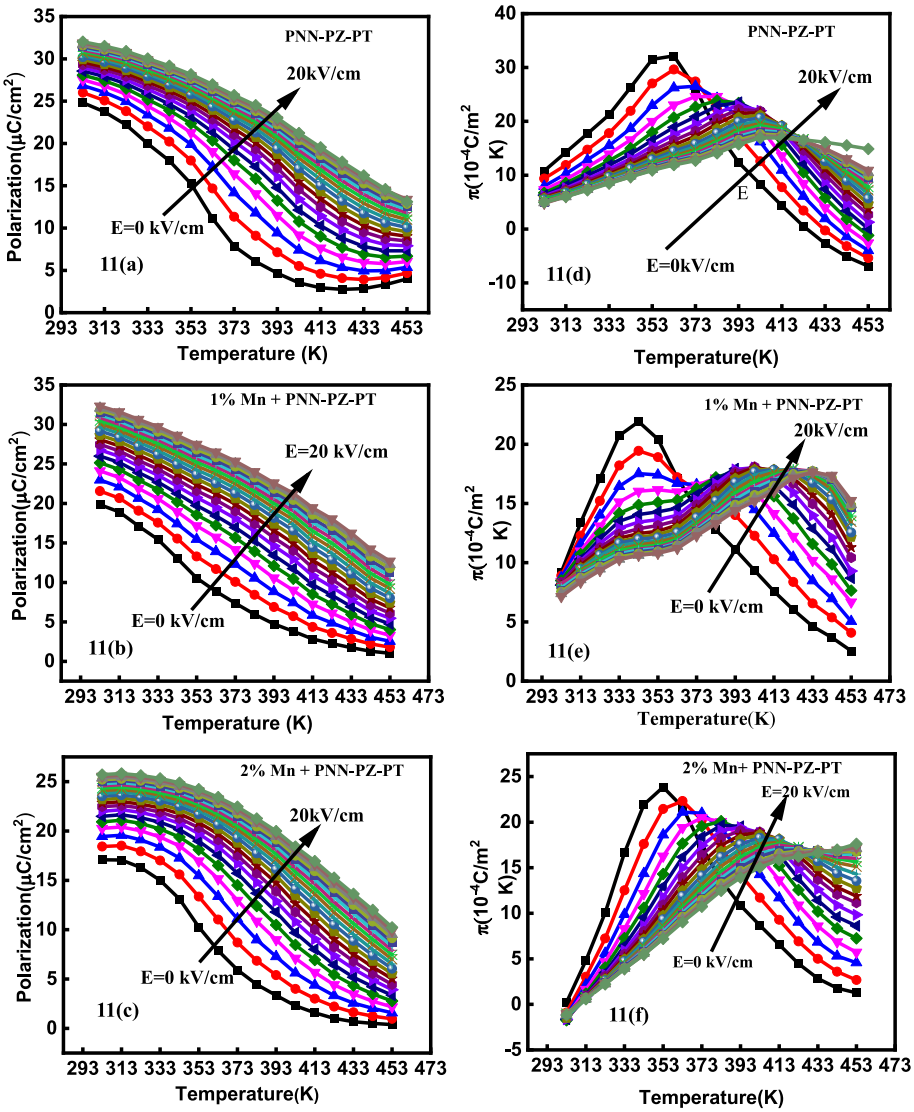

Fig. 11. (a–c) Polarization versus temperature curve as a function of electric field, (d)–(f) pyroelectric coefficient (dP/dT) versus temperature plots of PNN-PZ-PT ceramics sintered at different temperatures.

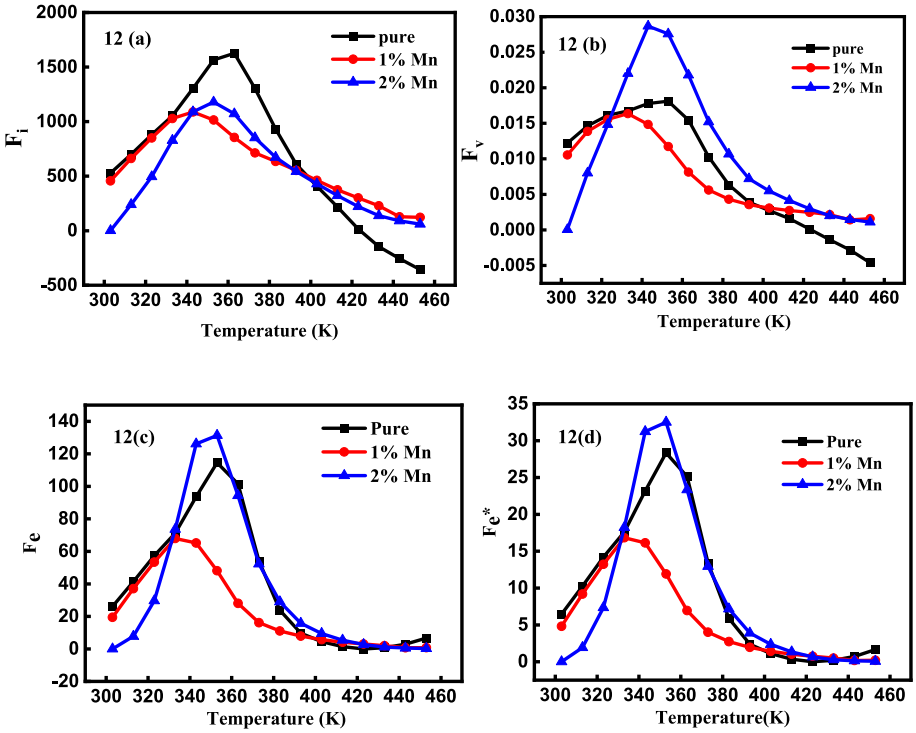

Fig. 12. (a–d) Pyroelectric figure of merits for xMn-PNN-PZ-PT ceramics in temperature range 300K- 450K.

Table 4
Comparison of room temperature figure of merits of other well-known materials with present work.

Compositions	π (10^{-4}C/m^2 K)	F_i (pm/V)	F_v (m^2/C)	F_e (J/m^{3}K^2)	F_e* (pm^3/J)	Reference
$PbNi_{0.183}Nb_{0.366}Zr_{0.135}Ti_{0.315}O_3$	10.86	533	0.012	26.51	6.46	This work
$PbNi_{0.183}Nb_{0.366}Zr_{0.135}Ti_{0.315}O_3$ +1 % Mn	9.18	456	0.010	20.04	4.89	This work
$PbNi_{0.183}Nb_{0.366}Zr_{0.135}Ti_{0.315}O_3$ +2 % Mn	0.03	9.95	0.001	0.64	0.04	This work
$PbNb_{0.02}(Zr_{0.95}Ti_{0.05})_{0.98}O_3$	7.90	–	0.088	–	–	65
$Bi_{0.5}(Na_{0.95}K_{0.05})_{0.5}]_{0.95}Ba_{0.05}TiO_3$	3.25	194.6	0.026	–	–	66
$(Ba_{0.84}Ca_{0.15}Sr_{0.01})(Ti_{0.90}Zr_{0.09}Sn_{0.01}O_3)$	11.16	479.3	0.013	–	–	67
$BaCe_{0.1}Ti_{0.9}O_3$	3.57	171	0.009	6.8	1.53	68
$Ba_{0.85}Sr_{0.15}TiO_3$	4.70	201	0.030	21.9	6.1	69
$Bi_{0.5}(Na_{0.94}K_{0.05}Li_{0.016})_{0.5}]_{0.95}Ba_{0.05}TiO_3$	3.60	220.5	0.029	–	–	66

Table 5
Figure of merit of synthesized ceramics at high temperature (below curie).

Composition	F_i (pm/V)	F_v (m^2/C)	F_e (J/m^3 K^2)	F_e^* (pm^3/J)	T (K)
PNN-PZ-PT	1637	0.018	115	28.41	~360
PNN-PZ-PT+1% Mn	1181	0.016	67.96	16.95	~335
PNN-PZ-PT+2% Mn	1103	0.026	132.03	32.508	~350

2 % Mn doped sample shows the optimal value of pyroelectric figure of merits values at elevated temperature (below T_c) i.e F_i = 1103 p.m./V, F_v = 0.026 m^2/C, F_e = 132.03 J/m^3 K^{2}and F_e* = 32.508 p.m.^{3}/J suggesting pyroelectric FOMs of MPB based compound can be enhanced by heterovalent doping. Our study highlights the significance of acceptor doping in optimizing select figures of merit. Further, to realize simultaneous improvements across all relevant FOM parameters of PNN-PZ-PT, precise doping and comprehensive characterization techniques are essential.

CRediT authorship contribution statement

Shubham Modgil: Writing – original draft, Methodology, Investigation, Formal analysis. **Mehak Aggarwal:** Formal analysis, Data curation. **Mukul Kumar:** Formal analysis, Data curation. **Arun Kumar Singh:** Writing – review & editing, Validation. **Shobhna Dhiman:** Supervision, Formal analysis. **Gyaneshwar Sharma:** Writing – review & editing, Validation, Investigation, Data curation. **Sanjeev Kumar:** Writing – review & editing, Supervision, Resources, Funding acquisition, Conceptualization.

Declaration of competing interest

The authors declare that they have no known competing financial interests or personal relationships that could have appeared to influence the work reported in this paper.

Acknowledgments

S.K. is grateful to the financial support received from ER&IPR, DRDO, Govt. Of India for generous funding through project (ERIP/ER/202206003/M/01/1804).

Data availability

Data will be made available on request.

References

[1] F. Guo, S. Zhang, W. Long, P. Fang, X. Li, Z. Xi, SnO_2 modified PNN-PZT ceramics with ultra-high piezoelectric and dielectric properties, Ceram. Int. 48 (16) (2022) 23241–23248, https://doi.org/10.1016/j.ceramint.2022.04.308.

[2] X. Li, W. Wu, Y. Chung, W.Y. Shih, W.H. Shih, Q. Zhou, K.K. Shung, 80-MHz intravascular ultrasound transducer using PMN-PT free-standing film, IEEE Trans. Ultrason. Ferroelectrics Freq. Control 58 (11) (2011) 2281–2288, https://doi.org/10.1109/TUFFC.2011.2085.

[3] D. Zabek, K. Seunarine, C. Spacie, C. Bowen, Graphene ink laminate structures on poly (vinylidene difluoride)(PVDF) for pyroelectric thermal energy harvesting and waste heat recovery, ACS Appl. Mater. Interfaces 9 (10) (2017) 9161–9167, https://doi.org/10.1021/acsami.6b16477.

[4] G. Sebald, E. Lefeuvre, D. Guyomar, Pyroelectric energy conversion: optimization principles, IEEE Trans. Ultrason. Ferroelectrics Freq. Control 55 (3) (2008) 538–551, https://doi.org/10.1109/TUFFC.2008.680.

[5] M. Kohli, C. Wuethrich, K. Brooks, B. Willing, M. Forster, P. Muralt, P. Ryser, Pyroelectric thin-film sensor array, Sensor Actuator Phys. 60 (1–3) (1997) 147–153, https://doi.org/10.1016/S0924-4247(97)01484-2.

[6] M. Noda, K. Inoue, M. Ogura, H. Xu, S. Murakami, H. Kishihara, M. Okuyama, An uncooled infrared sensor of dielectric bolometer mode using a new detection technique of operation bias voltage, Sensor Actuator Phys. 97 (2002) 329–336, https://doi.org/10.1016/S0924-4247(02)00046-8.

[7] R. Whatmore, W, Pyroelectric devices and materials. Reports on progress in physics 49 (12) (1986) 1335, https://doi.org/10.1088/0034-4885/49/12/002.

[8] L. Liu, X. Wu, X. Zhao, X. Feng, W. Jing, H. Luo, Pyroelectric performances of rhombohedral 0.42 Pb $(In_{1/2}Nb_{1/2})O_3$-0.3 Pb$(Mg_{1/3}Nb_{2/3})$ O_3-0.28 $PbTiO_3$ single crystals, IEEE Trans. Ultrason. Ferroelectrics Freq. Control 57 (10) (2010) 2154–2158, https://doi.org/10.1109/TUFFC.2010.1672.

[9] P. Yu, Y. Tang, H. Luo, Fabrication, property and application of novel pyroelectric single crystals—PMN–PT, J. Electroceram. 24 (2010) 1–4, https://doi.org/10.1007/s10832-007-9360-7.

[10] C.R. Bowen, J. Taylor, E. Le Boulbar, D. Zabek, V.Y. Topolov, A modified figure of merit for pyroelectric energy harvesting, Mater. Lett. 138 (2015) 243–246, https://doi.org/10.1016/j.matlet.2014.10.004.

[11] D.L. Polla, C.P. Ye, T. Tamagawa, Surface-micromachined $PbTiO_3$ pyroelectric detectors, Appl. Phys. Lett. 59 (27) (1991) 3539–3541, https://doi.org/10.1063/1.105650.

[12] J. Du, J. Qiu, K. Zhu, H. Ji, Microstructure, temperature stability and electrical properties of ZnO-modified Pb$(Ni_{1/3}Nb_{2/3})O_3$–Pb$(Fe_{1/2}Nb_{1/2})O_3$–Pb$(Zr_{0.3}Ti_{0.7})O_3$ piezoelectric ceramics, Ceram. Int. 39 (8) (Dec. 2013) 9385–9390, https://doi.org/10.1016/J.CERAMINT.2013.05.055.

[13] N. Luo, Q. Li, Z. Xia, Effect of Pb$(Fe_{1/2}Nb_{1/2})O_3$ modification on dielectric and piezoelectric properties of Pb$(Mg_{1/3}Nb_{2/3})O3$–$PbZr_{0.52}Ti_{0.48}O_3$ ceramics, Mater. Res. Bull. 46 (9) (Sep. 2011) 1333–1339, https://doi.org/10.1016/J.MATERRESBULL.2011.05.026.

[14] P.H. Kim, J.G. Lee, J.H. Cho, W.S. Kang, S.G. Lee, H.Y. Lee, W. Jo, In situ total strain measurements revealing the strain mechanism of Pb $(Mg_{1/3}Nb_{2/3})O_3$-$PbTiO_3$ single crystals, Journal of Materiomics 7 (4) (2021) 693–698, https://doi.org/10.1016/j.jmat.2020.09.002.

[15] S. Chandarak, M. Unruan, A. Prasatkhetragarn, R. Yimnirun, Structural investigation of PZT-PNN and PZT-PZN probed by synchrotron X-ray absorption spectroscopy, Ferroelectrics 455 (1) (Jan. 2013) 117–122, https://doi.org/10.1080/00150193.2013.845485.

[16] Y. Zhang, X. Zhu, J. Zhu, X. Zeng, X. Feng, J. Liao, Composition design, phase transitions and electrical properties of Sr^{2+}-substituted xPZN–0.1PNN–(0.9−x)PZT piezoelectric ceramics, Ceram. Int. 42 (3) (Feb. 2016) 4080–4089, https://doi.org/10.1016/J.CERAMINT.2015.11.080.

[17] C. Kornphom, A. Laowanidwatana, T. Bongkarn, Fabrication of pyrochlore phase free PMN-PZT ceramics via the combustion technique, Integrated Ferroelectrics Int. J. 165 (1) (Sep. 2015) 11–18, https://doi.org/10.1080/10584587.2015.1062338.

[18] W. Ruan, G. Li, J. Zeng, L.S. Kamzina, H. Zeng, L. Zheng, A. Ding, Fabrication of PMN–PZT transparent ceramics by two-stage sintering, J. Am. Ceram. Soc. 95 (7) (2012) 2103–2106, https://doi.org/10.1111/J.1551-2916.2012.05244.X.

[19] Q. Guo, F. Li, F. Xia, P. Wang, X. Gao, H. Hao, S. Zhang, Piezoelectric ceramics with high piezoelectricity and broad temperature usage range, Journal of Materiomics 7 (4) (2021) 683–692, https://doi.org/10.1016/j.jmat.2020.11.012.

[20] H.J. Fan, et al., Brillouin and dielectric studies of the phase transition in the relaxor ferroelectric Pb(Ni1/3Nb2/3)O3, J. Appl. Phys. 91 (4) (Feb. 2002) 2262–2266, https://doi.org/10.1063/1.1433183.

[21] Z. Li, L. Zhang, X. Yao, Preparation and dielectric properties for temperature-stable Pb $(Ni_{1/3}Nb_{2/3})O_3$-based composite ceramics, J. Mater. Sci. Lett. 17 (1998) 1921–1923, https://doi.org/10.1023/A:1006604308968.

[22] C.H. Lu, W.J. Hwang, Phasic and microstructural developments of Pb $(Ni_{1/3}Nb_{2/3})$ O_3 prepared by the columbite precursor process, Ceram. Int. 22 (5) (1996) 373–379, https://doi.org/10.1016/0272-8842(95)00116-6.

[23] S. Wirunchit, P. Laoratanakul, N. Vittayakorn, Physical properties and phase transitions in perovskite Pb [Zr1− x $(Ni_{1/3}Nb_{2/3})$ x] O_3 (0.0⩽ x⩽ 0.5) ceramics, J. Phys. Appl. Phys. 41 (12) (2008) 125406, https://doi.org/10.1088/0022-3727/41/12/125406.

[24] E.F. Alberta, A.S. Bhalla, Low-temperature properties of lead nickel-niobate ceramics, Mater. Lett. 54 (1) (May 2002) 47–54, https://doi.org/10.1016/S0167-577X(01)00538-9.

[25] D. Luff, R. Lane, B. Rr, M. Hj, in: Ferroelectric Ceramics with High Pyroelectric Properties, 1974 [Online]. Available:.

[26] J. Wu, Z. Hu, X. Gao, M. Cheng, X. Zhao, W. Su, M. Liu, Unconventional piezoelectric coefficients in perovskite piezoelectric ceramics, Journal of Materiomics 7 (2) (2021) 254–263, https://doi.org/10.1016/j.jmat.2020.10.004.

[27] W. Peng, J. Chang, J. Zhao, D. Wang, Z. Liu, G. Wang, S. Dong, Enhanced piezoelectric properties and thermal stability of LiNbO3-modified PNN–PZT ceramics, Journal of Materiomics (2023), https://doi.org/10.1016/j.jmat.2023.10.013.

[28] H. Liu, et al., Effect of MnO_2 doping on piezoelectric, dielectric and ferroelectric properties of PNN–PZT ceramics, Ceram. Int. 41 (9) (Nov. 2015) 11359–11364, https://doi.org/10.1016/J.CERAMINT.2015.05.094.

[29] G. Peng, C. Chen, J. Zhang, D. Zheng, S. Hu, H. Zhang, Effects of PNN/PZT ratios on phase structure, electric properties and relaxation behavior of PZN–PNN–PZT ceramics, J. Mater. Sci. Mater. Electron. 27 (4) (Apr. 2016) 3145–3151, https://doi.org/10.1007/S10854-015-4136-3/METRICS.

[30] F. Guo, S. Zhang, W. Long, P. Fang, X. Li, Z. Xi, SnO_2 modified PNN-PZT ceramics with ultra-high piezoelectric and dielectric properties, Ceram. Int. 48 (16) (Aug. 2022) 23241–23248, https://doi.org/10.1016/J.CERAMINT.2022.04.308.

[31] S.H. Kang, D.S. Lee, S.Y. Lee, I.W. Kim, J.S. Kim, E.C. Park, J.S. Lee, Pyroelectric and piezoelectric properties of yttrium-doped 0.15 [Pb$(Ni_{1/3}Nb_{2/3})O_3$]–0.85[Pb$(Zr_{1/2}Ti_{1/2})O_3$] ceramics, Ceram. Int. 30 (7) (2004) 1453–1457, https://doi.org/10.1016/j.ceramint.2003.12.159.

[32] J.F. Scott, C.A. Araujo, B.M. Melnick, L.D. McMillan, R. Zuleeg, Quantitative measurement of space-charge effects in lead zirconate-titanate memories, J. Appl. Phys. 70 (1) (1991) 382–388, https://doi.org/10.1063/1.350286.

[33] J.F. Scott, B.M. Melnick, C.A. Araujo, L.D. McMillan, R. Zuleeg, DC leakage currents in ferroelectric memories, Integrated Ferroelectrics Int. J. 1 (2–4) (1992) 323–331, https://doi.org/10.1080/10584589208215720.

[34] Q. Zhang, Y. Zhang, T. Yang, X. Yao, High antiferroelectric stability and large electric field–induced strain in MnO_2-doped $Pb_{0.97}La_{0.02}(Zr_{0.63}Sn_{0.26}Ti_{0.11})O_3$ ceramics, J. Intell. Mater. Syst. Struct. 25 (4) (2014) 501–505, https://doi.org/10.1177/1045389X13498.

[35] J. Yoo, S. Lee, Piezoelectric properties of MnO_2 doped low temperature sintering Pb$(Mn_{1/3}Nb_{2/3})O_3$-Pb$(Ni_{1/3}Nb_{2/3})O_3$-Pb$(Zr_{0.50}Ti_{0.50})O_3$ ceramics, J. Electroceram. 23 (2–4) (Oct. 2009) 432–436, https://doi.org/10.1007/S10832-008-9483-5/METRICS.

[36] P. Qiao, Y. Zhang, X. Chen, M. Zhou, G. Wang, X. Dong, Effect of Mn-doping on dielectric and energy storage properties of $(Pb_{0.91}La_{0.06})(Zr_{0.96}Ti_{0.04})O_3$ antiferroelectric ceramics, J. Alloys Compd. 780 (2019) 581–587, https://doi.org/10.1016/j.jallcom.2018.11.371.

[37] Q. Zhang, R.W. Whatmore, Sol-gel PZT and Mn-doped PZT thin films for pyroelectric applications, J. Phys. Appl. Phys. 34 (15) (2001) 2296, https://doi.org/10.1088/0022-3727/34/15/308.

[38] H. Wei, Y. Chen, Ferroelectric and pyroelectric properties of Mn-doped lead zirconate titanate ceramics, Ceram. Int. 41 (5) (2015) 6158–6163, https://doi.org/10.1016/j.ceramint.2014.02.113.

[39] P. Qiao, Y. Zhang, X. Chen, M. Zhou, G. Wang, X. Dong, Enhancing pyroelectric properties in $(Pb_{1-1.5x}La_x)(Zr_{0.86}Ti_{0.14})O_3$ ceramics through composition modulated phase transition, Ceram. Int. 45 (6) (2019) 7114–7119, https://doi.org/10.1016/j.ceramint.2018.12.216.

[40] C. Wu, W. Gong, J. Geng, J. Cui, L. Mi, J. Nie, F.Z. Yao, Effects of Mn-doping on the structure and electrical properties of Sm-PMN-PT piezoceramics, Journal of Advanced Dielectrics 13 (3) (2023) 2350004.

[41] http://abulafia.mt.ic.ac.uk/shannon/.

[42] L. Bian, X. Qi, K. Li, J. Fan, Z. Li, E. Sun, W. Cao, High-performance Pb $(Ni_{1/3}Nb_{2/3})$ O_3-$PbZrO_3$-$PbTiO_3$ ceramics with the triple point composition, J. Eur. Ceram. Soc. 41 (14) (2021) 6983–6990, https://doi.org/10.1016/J.JEURCERAMSOC.2021.07.034.

[43] T.G. Lee, H.J. Lee, D.H. Kim, H. Xu, S.J. Park, J.S. Park, S.J. Yoon, Relation between structure and piezoelectric properties of (1-xy)$PbZrO_3$-x$PbTiO_3$-yPb$(Ni_{1/3}Nb_{2/3})O_3$ ceramics near triple point composition, J. Eur. Ceram. Soc. 36 (16) (2016) 4049–4057, https://doi.org/10.1016/J.JEURCERAMSOC.2016.07.014.

[44] Y. Zhang, H. Liu, S. Sun, S. Deng, J. Chen, Systematic study of structure and piezoelectric properties of Pb$(Ni_{1/3}Nb_{2/3})O_3$-$PbTiO_3$ by in situ synchrotron diffraction, J. Am. Ceram. Soc. 104 (1) (Jan. 2021) 604–612, https://doi.org/10.1111/JACE.17472.

[45] H. Liu, J. Chen, L. Fan, Y. Ren, Z. Pan, K.V. Lalitha, X. Xing, Critical role of monoclinic polarization rotation in high-performance perovskite piezoelectric materials, Phys. Rev. Lett. 119 (1) (2017) 017601, https://doi.org/10.1103/PHYSREVLETT.119.017601/FIGURES/3/MEDIUM.

[46] J. Miao, Z. Zhang, Z. Liu, Y. Li, Investigation on the dielectric properties of Mg-doped $(Ba_{0.95}Ca_{0.05})(Ti_{0.85}Zr_{0.15})O_3$ ceramics, Ceram. Int. 41 (S1) (Jul. 2015) S487–S491, https://doi.org/10.1016/J.CERAMINT.2015.03.302.

[47] P. Jaiban, A. Watcharapasorn, R. Yimnirun, R. Guo, A.S. Bhalla, Effects of donor and acceptor doping on dielectric and ferroelectric properties of $Ba_{0.7}Ca_{0.3}TiO_3$ lead-free ceramics, J. Alloys Compd. 695 (Feb. 2017) 1329–1335, https://doi.org/10.1016/J.JALLCOM.2016.10.274.

[48] S. Priya, K. Uchino, Dielectric and piezoelectric properties of the Mn-substituted Pb $(Zn_{1/3}Nb_{2/3})O_3$–$PbTiO_3$ single crystal, J. Appl. Phys. 91 (7) (Apr. 2002) 4515–4520, https://doi.org/10.1063/1.1459101.

[49] E. Perez-Delfin, J.E. García, D.A. Ochoa, R. Pérez, F. Guerrero, J.A. Eiras, Effect of Mn-acceptor dopant on dielectric and piezoelectric responses of lead lanthanum zirconate titanate piezoceramics, J. Appl. Phys. 110 (3) (Aug. 2011), https://doi.org/10.1063/1.3622338.

[50] B.H. Watson III, M.J. Brova, M. Fanton, R.J. Meyer Jr., &G.L. Messing, Textured Mn doped PIN-PMN-PT ceramics: harnessing intrinsic piezoelectricity for high-power transducer applications, J. Eur. Ceram. Soc. 41 (2) (2021) 1270–1279, https://doi.org/10.1016/j.jeurceramsoc.2020.07.071.

[51] C. Wang, L. Ning, Y. Li, F. Li, $MnCO_3$ modified PMN-PZT piezoelectric ceramics with enhancing mechanical quality factor and low loss, Ceram. Int. 50 (7) (2024) 10835–10842, https://doi.org/10.1016/j.ceramint.2023.12.399.

[52] K. Uchino, S. Nomura, Critical exponents of the dielectric constants in diffused-phase-transition crystals, Ferroelectrics 44 (1) (Apr. 1982) 55–61, https://doi.org/10.1080/00150198208260644.

[53] L. Chen, R. Liang, G. Wang, H. Nie, Z. Zhou, F. Cao, &X. Dong, Poling induced dielectric anomalies in a PZT ceramic, Ceram. Int. 39 (8) (2013) 8941–8944, https://doi.org/10.1016/j.ceramint.2013.04.090.

[54] Y. Wang, P. Wang, L. Liu, Y. Wang, Y. Zhao, W. Tian, J. Shi, Defect dipole behaviors on the strain performances of bismuth sodium titanate-based lead-free piezoceramics, Materials 16 (11) (2023) 4008, https://doi.org/10.3390/ma16114008.

[55] C. He, Z. Wang, X. Li, X. Yang, X. Long, Z.G. Ye, Self-polarized high piezoelectricity and its memory effect in ferroelectric single crystals, Acta Mater. 125 (2017) 498–505, https://doi.org/10.1016/j.actamat.2016.12.017.

[56] R. Syal, R. Goel, A. De, A.K. Singh, G. Sharma, O.P. Thakur, S. Kumar, Flattening of free energy profile and enhancement of energy storage efficiency near morphotropic phase boundary in lead-free BZT-xBCT, J. Alloys Compd. 873 (2021) 159824, https://doi.org/10.1016/j.jallcom.2021.159824.

[57] C. Li, B. Xu, D. Lin, S. Zhang, L. Bellaiche, T.R. Shrout, F. Li, Atomic-scale origin of ultrahigh piezoelectricity in samarium-doped PMN-PT ceramics, Phys. Rev. B 101 (14) (2020) 140102, https://doi.org/10.1103/PhysRevB.101.140102.

[58] C. Wang, B. Fang, D. Wu, S. Zhang, J. Ding, Pyroelectric performance, dielectric response and conductive mechanism of BCHT lead-free piezoelectric ceramics via powder injection molding, J. Mater. Res. Technol. 9 (5) (Sep. 2020) 11303–11310, https://doi.org/10.1016/J.JMRT.2020.08.006.

[59] H. He, X. Lu, E. Hanc, C. Chen, H. Zhang, L. Lu, Advances in lead-free pyroelectric materials: a comprehensive review, J Mater Chem C Mater 8 (5) (Feb. 2020) 1494–1516, https://doi.org/10.1039/C9TC05222D.

[60] A. Kleiner, G. Suchaneck, A. Eydam, G. Gerlach, L. Liu, A. Günther, N. Neumann, Mn-doped PMN-PT thin films for electrocaloric applications, in: 2015 Joint *IEEE International Symposium On the Applications Of Ferroelectric (ISAF), International Symposium on Integrated Functionalities (ISIF), and Piezoelectric Force Microscopy Workshop* (PFM), IEEE, 2015, May, pp. 200–202, https://doi.org/10.1109/ISAF.2015.7172705.

[61] M. Aggarwal, A.K. Singh, G. Sharma, S. Dhiman, S. Kumar, Modulation of polar dynamics with oxygen vacancies in Zn doped $BaZr_{0.1}Ti_{0.9}O_3$, J. Alloys Compd. 927 (Dec. 2022) 166957, https://doi.org/10.1016/J.JALLCOM.2022.166957.

[62] M. Venet, I.A. Santos, J.A. Eiras, D. Garcia, Potentiality of SBN textured ceramics for pyroelectric applications, Solid State Ionics 177 (5–6) (Feb. 2006) 589–593, https://doi.org/10.1016/J.SSI.2005.12.006.

[63] K.K. Bajpai, K. Sreenivas, A.K. Gupta, A.K. Shukla, Pyroelectric properties of $(Ba_{1-x}Cd_x)(Zr_{0.13}Ti_{0.87})O_3$ ferroelectric ceramics in polymorphic state, Ceram. Int. 44 (12) (Aug. 2018) 14698–14703, https://doi.org/10.1016/J.CERAMINT.2018.05.097.

[64] X. Chen, S. Yan, H. Nie, F. Cao, G. Wang, X. Dong, Improved pyroelectric figures of merit of Mn-doped Zr-rich lead zirconate titanate bulk ceramics near room temperature for energy harvesting applications, J. Alloys Compd. 779 (2019) 450–455, https://doi.org/10.1016/j.jallcom.2018.11.273.

[65] H. Wei, Y. Chen, Ferroelectric and pyroelectric properties of Mn-doped lead zirconate titanate ceramics, Ceram. Int. 41 (5) (2015) 6158–6163, https://doi.org/10.1016/j.ceramint.2014.02.113.

[66] S.T. Lau, C.H. Cheng, S.H. Choy, D.M. Lin, K.W. Kwok, H.L. Chan, Lead-free ceramics for pyroelectric applications, J. Appl. Phys. 103 (10) (2008), https://doi.org/10.1063/1.2927252.

[67] X. Liu, D. Wu, Z. Chen, B. Fang, J. Ding, X. Zhao, H. Luo, Ferroelectric, dielectric and pyroelectric properties of Sr and Sn codoped BCZT lead free ceramics, Adv. Appl. Ceram. 114 (8) (2015) 436–441, https://doi.org/10.1179/1743676115Y.0000000015.

[68] K.S. Srikanth, R. Vaish, Enhanced electrocaloric, pyroelectric and energy storage performance of BaCexTi1− xO3 ceramics, J. Eur. Ceram. Soc. 37 (13) (2017) 3927–3933, https://doi.org/10.1016/j.jeurceramsoc.2017.04.058.

[69] K.S. Srikanth, V.P. Singh, R. Vaish, Pyroelectric performance of porous $Ba_{0.85}Sr_{0.15}TiO_3$ ceramics, Int. J. Appl. Ceram. Technol. 15 (1) (2018) 140–147, https://doi.org/10.1111/ijac.12764.